CrossMark

Sol–gel synthesis and room temperature ferromagnetism in Mn doped ZnO nanocrystals

K. Omri[1] · O. M. Lemine[2] · J. El Ghoul[1,2] · L. El Mir[1,2]

Abstract We report the synthesis of $Zn_{1-x}Mn_xO$ nanoparticles prepared by a sol–gel processing technique for x ranging from 0 to 0.05. The structural, morphological and magnetic properties of the nanoparticles were investigated by XRD, transmission electron microscopy and superconducting quantum interference device. The structural properties showed that the obtained nanoparticles are in wurtzite phase structure with the presence of $ZnMnO_3$ secondary phase at higher concentration. The crystallite size decreases with increasing Mn concentration and is in the range of 35–17 nm. All the samples are ferromagnetic with clear hysteresis loop at room temperature but with low values for the saturation. It was found that increasing Mn concentration is not helping the long range ferromagnetic order, which might be due to the antiferromagnetic exchanges. This ferromagnetism order is due mainly to the defects and to the substituting of Mn in the ZnO host rather than from the secondary phases of Mn.

1 Introduction

In the last years, the semiconductor materials, especially II–VI semiconductors have attracted great interest due to their unique properties and potential applications [1]. Specially, zinc oxide (ZnO) as a semiconductor with a wide band gap (3.3 eV), large exciton binding energy of 60 meV at room temperature (RT) [2], abundant in nature and environmentally friendly; these characteristics make this material attractive for many applications such as solar cells, optical coatings, photocatalysts, antibacterial activities, electrical devices, active medium in UV semiconductor lasers and in gas sensors [3]. Among all the transition metal (TM) elements, the doping of ZnO by Mn is most encouraging because doping element has the highest possible magnetic moment and also the first half of the d-band is full, creating a stable fully polarized state [4]. Zinc oxide in hexagonal wurtzite crystal phase is a promising material for manufacturing photodetectors, blue and ultraviolet laser diodes [5], transparent field effect transistors, etc. Many researchers are still trying to obtain experimental proofs for such ferromagnetism in powder, bulk and thin films of transition-metal-doped ZnO. However, ZnO thin films have been used in gas sensors [6, 7], solar cell transparent contact fabrications [8], surface acoustic wave systems [9] and UV laser [10]. Another interesting application of ZnO is in the field of spintronics which is an emerging field in physics focused on spin-dependent phenomena applied to modern electronic devices [11]. Diluted magnetic semiconductors (DMS), which combine the two interesting properties: semiconducting and magnetic, are considered as an ideal system for spintronics [12, 13]. Mn-doped ZnO nanocrystals are a good candidate for the fabrication of transparent spintronics devices. It's transparent in the visible region and the thermal equilibrium solubility of Mn in ZnO is larger than 10 mol% [14]. For this reasons, Mn doped ZnO nanocrystals has attracted an increasing interest and several works reported RT ferromagnetic behavior [15–23]. However, the correct mechanism of this RT ferromagnetism behavior is still a topic of debate.

✉ O. M. Lemine
leminej@yahoo.com

1 Laboratory of Physics of Materials and Nanomaterials Applied at Environment (LaPhyMNE), Faculty of Sciences of Gabes, Gabes University, 6072 Gabès, Tunisia

2 Department of Physics, College of Sciences, Al Imam Mohammad Ibn Saud Islamic University (IMSIU), Riyadh 11623, Saudi Arabia

Motivated by our recent work on the synthesis and the optical properties of this system [24] and also in order to contribute to the debate regarding the origin of the ferromagnetism in TM doped ZnO nanocrytsals, we report the effect of manganese as TM doping element on structural and magnetic properties of ZnO nanocrystals synthesised by sol–gel methods.

2 Experimental procedure

2.1 Synthesis details

The sample preparation processes have been reported in our previous works [24, 25]. For the synthesis of the samples, we dissolved 2 g of zinc acetate dehydrate in 14 ml of methanol under magnetic stirring for 2 h and then we added of manganese (II) chloride-4-hydrate corresponding to [Mn]/([Zn] + [Mn]) at different Mn doping concentrations (1 at.%, 2 at.%, 3 at.%, 4 at.% and 5 at.%), with stirring until complete dissolution of the precursors. Then, the resulting solution underwent rapid drying to obtain aerogel powder. Finally, we conducted drying in supercritical conditions of ethanol, with a heating rate of 45 °C/h.

2.2 Characterization

The crystalline phases of the obtained nanopowders were identified by X-ray diffraction (XRD) using a Bruker D5005 powder X-ray diffractometer using a CuKα source (1.5418 Å radiation). It is known that XRD line broadening is influenced by the crystallite size and the internal strains. In order to obtain these parameters, Williamson–Hall and Scherrer methods were used. In the Williamson–Hall method, the analysis includes two steps:

First step: the width (β_{exp}) of every peak was measured as the integral breadth. The instrumental broadening (β_{inst}) was determined from polycrystalline silicon standard. The peak breadth due to sample (strain + size), B was calculated according to Gaussian profile:

$$B^2 = \beta_{exp}^2 - \beta_{inst}^2 \tag{1}$$

Second step: the crystalline size and internal strain were obtained by fitting the Williamson–Hall equation:

$$B \cos\theta = \frac{K\lambda}{D} + 4\varepsilon \sin\theta \tag{2}$$

where D is the coherent scattering length (crystalline size); K is a constant whose value is approximately 0.9; B the integral width of the sample (in rad) calculated in the first step and ε the inhomogeneous internal strain (in %). Crystallite sizes (G, in Å) were estimated from the Scherrer's equation [26]:

$$G = \frac{0.9\lambda}{B \cos\theta_B} \tag{3}$$

where λ is the X-ray wavelength (1.5418 Å), θ_B is the maximum of the Bragg diffraction peak (in radians) and B is the linewidth at half maximum.

Transmission electron microscopy (TEM, JEM-200CX) were used to study the morphology and particle size of the phosphor powders. The specimens for TEM were prepared by putting the as-grown products in EtOH and immersing them in an ultrasonic bath for 15 min, then dropping a few drops of the resulting suspension containing the synthesized materials onto TEM grid. The magnetic properties of the samples were characterized by a commercial Quantum Design SQUID-VSM magnetometer. All the powder samples enwrapped by quite low magnetic background parafilms were mounted inside the standard brass sample holder for magnetic measurements. Field dependent magnetizations up to 6 Tesla have been measured at room temperature.

3 Results and discussion

Figure 1 shows typical XRD spectra of the ZnO:Mn powders with different Mn doping concentrations. In the case of undoped ZnO, we noticed the appearance of nine pronounced diffraction peaks at 2θ = 31.50°, 34.19°, 36.15°, 47.39°, 56.44°, 62.79°, 67.93°, 68.91°, 72.33°, 76.97°, 89.41° and 95.31° which can be attributed to the (100), (002), (101), (102), (110), (013), (112), (201), (022), (023) and (211) planes of ZnO, respectively [18]. The obtained XRD spectra matched well with the space group P6₃mc (186) (No. 36-1451) of wurtzite ZnO structure [18,
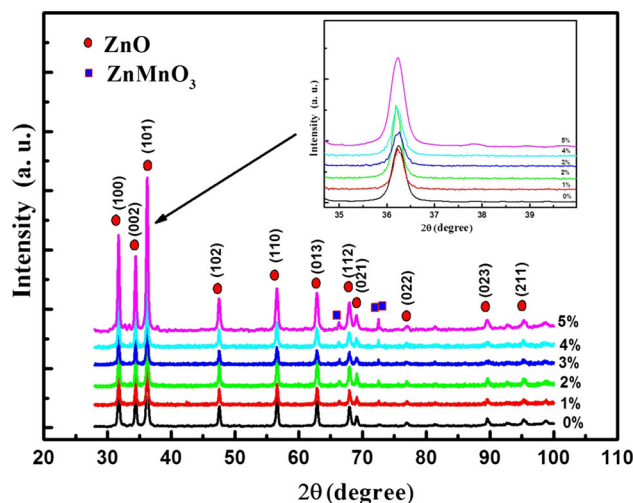

Fig. 1 X-ray diffractograms of ZnO:Mn nanoparticles for different manganese doping concentrations

24]. After doping of ZnO with manganese, in addition to the peaks corresponding to ZnO, one secondary additional phase were detected which can be attributed to ZnOMn$_3$, (JCPDS Card 37-1485). The lattice constants calculated from the XRD pattern, which are very close to ZnO ones, i.e., $a = 3.2493$ Å and $c = 5.2061$Å. These results are in a good agreement with our previous works [18, 24, 25].

In addition, a shift of peak positions was observed which is generally related to the expansion of unit cell volume. The dependence of lattices parameters and unit cell volume are presented in Fig. 2a and b respectively. It can be seen a linear increase of the cell volume with doping concentration. This is probably due to the substitution of the relatively large ionic radii Mn^{2+} (0.080 nm) ions at the smaller radii Zn^{2+} (0.074 nm) sites expands the lattice parameter, leading to a small increase in the c-axis lattice constant with the Mn content [18, 27, 28]. A similar increase in the lattice parameters has been reported for (ZnO:Mn) by various researchers [14, 29, 30]. It is desirable in DMS that the doping atom must substitute the ions of the host lattice. In ZnO system, dopants of 2+ oxidation state mostly substitute the Zn^{2+} ions in the lattice due to charge matching. In case of manganese doping, the ionic radius of Mn^{2+} (0.80 Å) ion is quite bigger than the Zn^{2+}

(0.74 Å) ion [31]. If Mn^{2+} ion substitutes Zn^{2+} ion in the lattice then the change in the lattice parameters is expected due to ionic radii mismatch which has also been reported by others [30]. Upon doping with 5 % manganese, the resultant compound maintains a wurtzite structure, but the lattice parameters 'a' and 'c' are both slightly increased in comparison to undoped ZnO. Additionally, the observed shrink of the cell parameters as manganese concentration goes up from 1 to 5 %, reflects migration of Mn ions from the wurzite structure to ZnOMn$_3$ impurity phase [29].

On the other hand, with increasing the Mn doping content, the diffraction peaks became broadened and their relative intensity decreases. This is due to the reduction of crystallites size and lattice strain. Both values were obtained by using Williamson–Hall method. The six most intensive reflection peaks of the samples were used in the line broadening analysis. Figure 3 shows Williamson–Hall plot for our samples doped at 0.0 at.%, 2 at.%, 3 at.% and 5 at.% of Mn. From these curves we can estimated the crystalline size (intercept at $\sin\theta = 0$, from the Eq. 2), and internal strain (slop). In addition, the crystallite size was calculated from Scherer's formula (Eq. 3) using the most intense peak (101). For increasing concentration of Mn, the average grain size decrease from 34 to 17 nm with an increase concentration of Mn.

Figure 4 shows the evolution of crystallite size with increasing Mn doping content obtained by both methods. We noticed that the crystallite size decreases with increasing Mn doping. This behavior is explained by the formation of defects during the sol–gel method process and has been reported previously [32, 33]. This may be attributed to various factors: (1) Mn^{2+} has larger ionic radius than Zn^{2+} (0.80 Å and 0.74 Å) hence its substitution during synthesis will create some strains/stresses within the crystal lattice; (2) Mn can promote both densification and grain growth; (3) increased grain boundaries or surface diffusion; etc. Bououdina et al. [33] reported similar results for higher concentration of Mn. It is important also to notice that the internal strain increase but start to decrease at high concentration (Fig. 5). The decreases of strain for high concentration not totally understood but we will see later that can be correlated with the changes in the magnetic properties and may be related to the defects.

Figure 6a shows TEM image of Mn doped ZnO nanopowders. It is shown that very small particles of ZnO:Mn are present in this powder as prepared in the first step. The crystallites present a very similar prismatic shape with a narrow particle size distribution. The majority of ZnO particles present in this powder have a size of about 35 nm, in a good agreement with the particle sizes deduced from XRD spectra [18, 25]. Energy dispersive spectroscopy (EDX) analysis (Fig. 6b) confirms the presence of Mn, Zn and O elements.
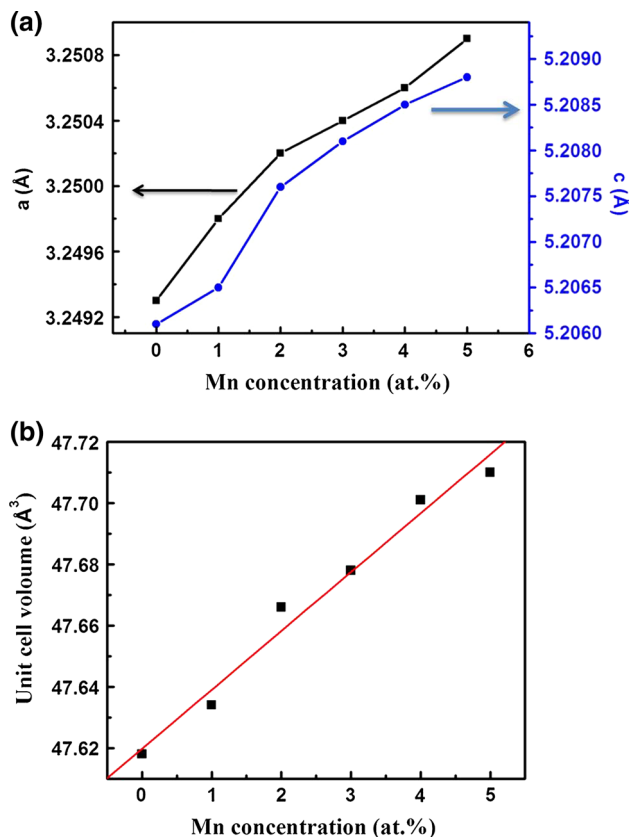

Fig. 2 Dependance on Mn concentration of **a** Lattice parameters and **b** Unit cell volume
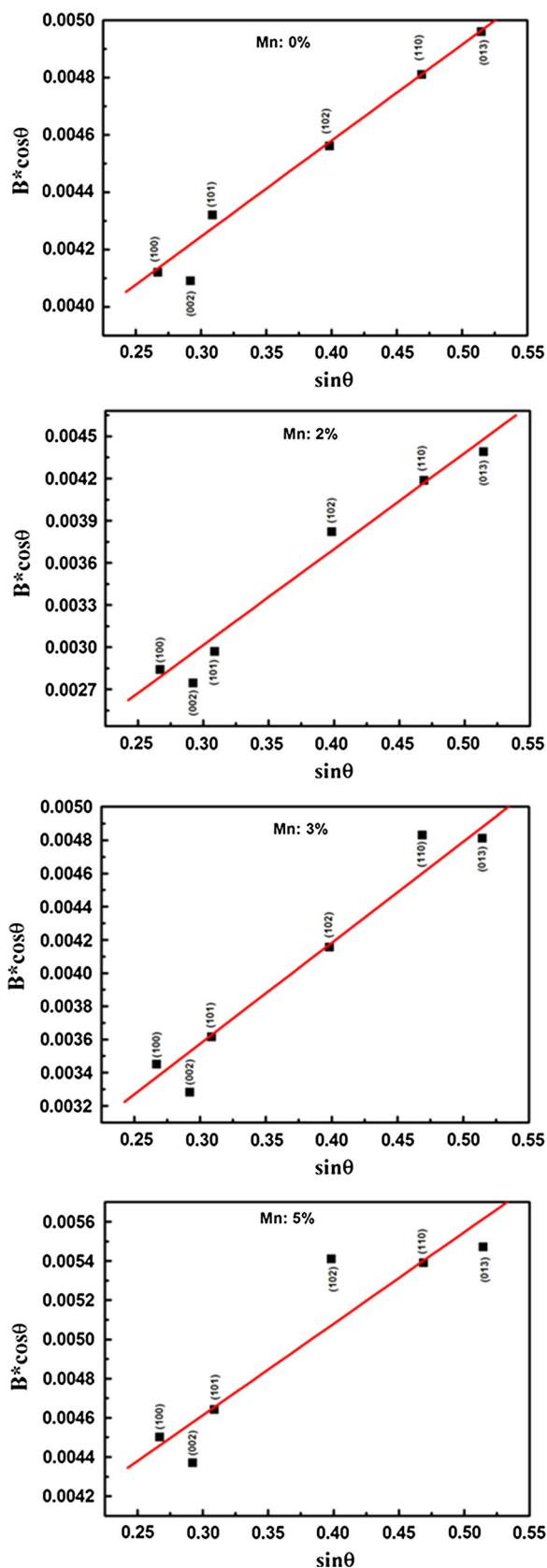
Fig. 3 Williamson–Hall plot showing X-ray peak broadening (B) as function of Bragg angle (θ) for our samples
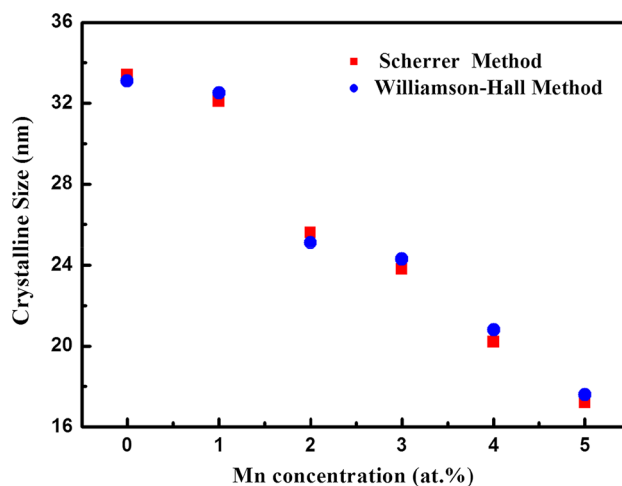

Fig. 4 The crystalline size obtained by Williamson–Hall and Scherrer method for different manganese doping concentrations
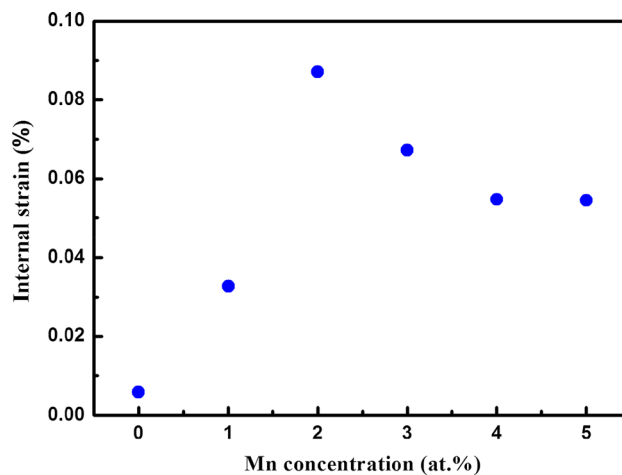

Fig. 5 The variation of internal strain for our samples

Figure 7a represents the M–H curves at RT for the Mn-doped ZnO samples with different Mn concentrations. The curves show that there is a ferromagnetic component superimposed on strong diamagnetic and paramagnetic backgrounds (Fig. 7a). After subtraction of the diamagnetic contribution (inset Fig. 7b), the ferromagnetism hysteresis curve is clearly observed for the samples (Fig. 7b). The magnetic parameters deduced after subtraction of dia-magnetic contribution are summarized in Table 1. The highest saturation magnetization (M_s) value (0.00254 emu/g) is obtained for 1 % Mn concentration and decreases with increasing Mn concentration except for 5 % Mn concentration. This decrease of the saturation magnetization with increasing Mn concentration can be attributed to the possible antiferromagnetism order between nearest neighbor of Mn–Mn atoms. Decreased Mn–Mn distance due to the
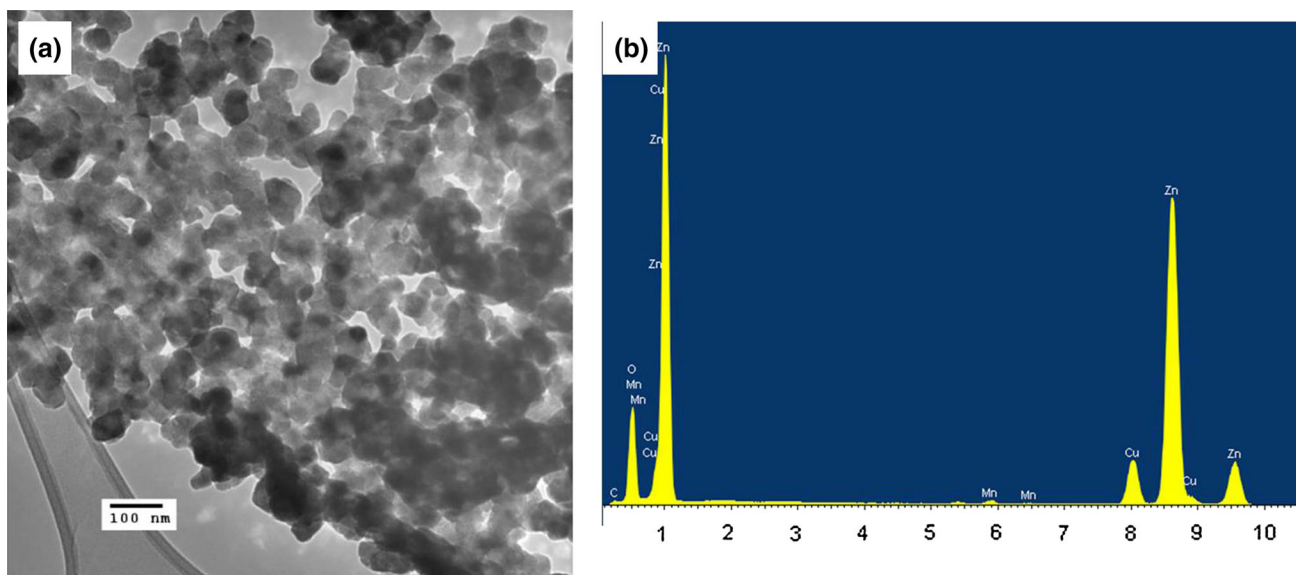
Fig. 6 a Typical TEM photograph showing the general morphology of ZnO:Mn nanoparticles and **b** EDX analysis of ZnO:Mn nanoparticles
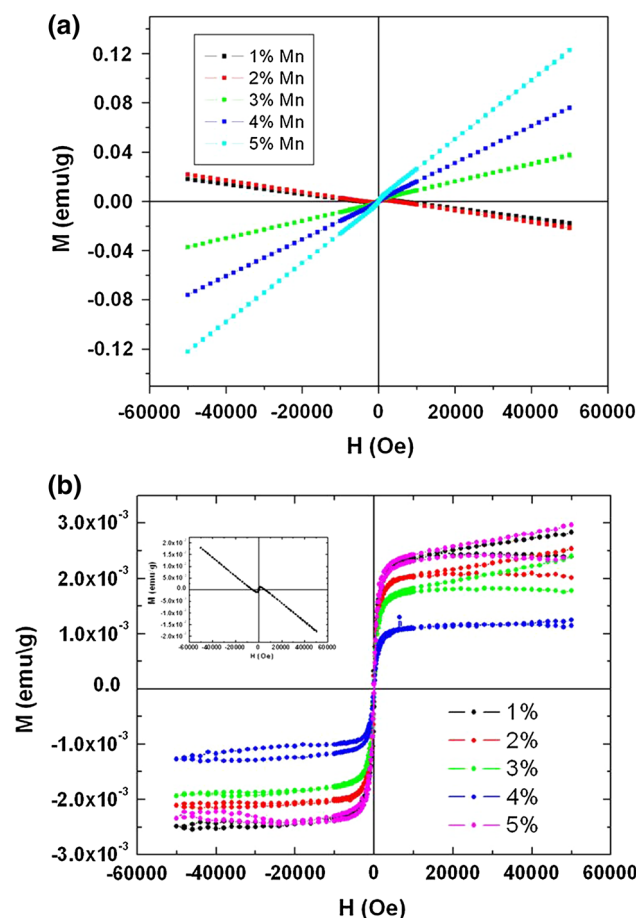

Fig. 7 Field dependent M–H curves at 300 K **a** as measured and **b** after subtraction of diamagnetic contribution

Table 1 The magnetic parameters for different Mn concentration obtained at room temperature

Mn (at.%)	Ms (emu/g)	Mr (emu/g)	Hc (Oe)
1	0.00254	0.00232	100
2	0.00217	0.00201	96.7
3	0.00199	0.00175	72.4
4	0.00121	0.00111	74.5
5	0.00254	0.00232	30

increase of number of Mn atoms will lead to antiferromagnetic exchanges [23]. The decreases in the saturation can be also explained by the largest paramagnetic contribution for high Mn concentration. May be there are also some isolated Mn atoms which are paramagnetic in nature and that increases the paramagnetic contribution for increasing concentration. Similar behavior and magnetization values for Mn-doped ZnO for comparable concentration have been reported in the literature [32, 34, 35]. On the other hand, the coercive field decreases with increasing concentration (Fig. 8). Our result is similar with others reports where M_S and H_c changes have the same behavior [36–38]. Chattopadhyay et al. [39]. reported opposite trends of M_S and H_c for similar Mn concentrations. They claimed that such behavior is characteristic of soft ferromagnetic but they consider also that both behaviors can be explained by defects.

Figure 9 shows the temperature-dependent magnetization (M–T) of zero-field-cooled (ZFC) at an applied uni-
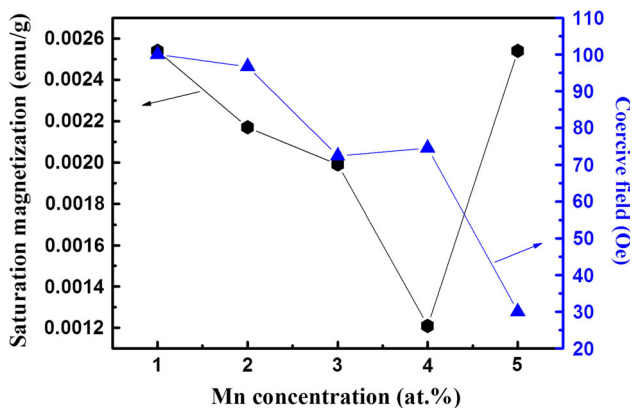
Fig. 8 Variation with Mn concentration for saturation magnetization and coercive field

form external field of 99.93 Oe and temperature range of 0–300 K for ZnO:Mn$_3$ % and ZnO:Mn$_4$ % samples. Small bifurcation has been observed up to 75 K for (M–T) curves. Notice that the shape of (M–T) curve (Fig. 9) is the same for both ZnO:Mn$_3$ % and ZnO:Mn$_4$ % samples. As shown by temperature-dependent magnetization curve of our samples, the magnetization decreases with increase of temperature. An abrupt decrease in magnetization values, which can be associated to magnetic phase change. The observations of the hysteresis loop and the abrupt decrease in magnetization indicate that a ferromagnetic phase with a Curie temperature above RT presents in our samples. The peak in both (M–T) curves indicates a transition at temperature around 26 K. This transition may be associated with the Mn induced defect incorporation in the system. It has been confirmed from XRD measurements that Mn related defect states increases with increase of Mn content.
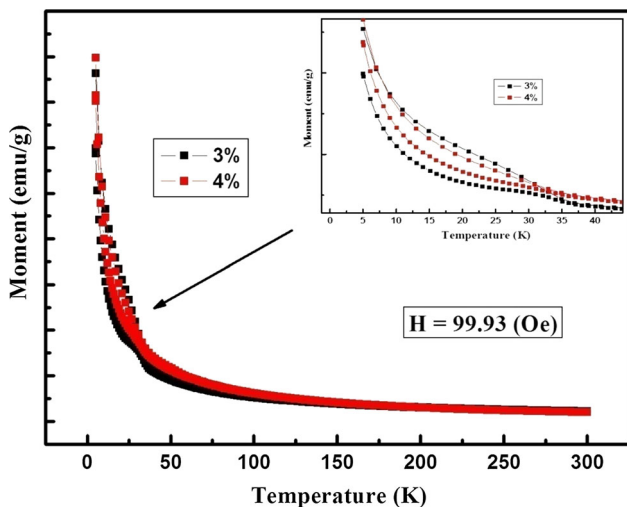

Fig. 9 M–T curves of ZnO:Mn$_3$ % and ZnO:Mn$_4$ % nanoparticles

The origin of the ferromagnetism in our samples can be explained based on the ferromagnetism mechanism in Mn doped ZnO system which is a topic of debate and not totally understood. Several authors reported that the ferromagnetism in Mn doped ZnO is an intrinsic property of the system [40, 41]. Other works consider that the ferromagnetism is due to the secondary phases such as MnO, Mn$_3$O$_4$, ZnMn$_2$O$_4$, etc. [42]. In our case, XRD shows the presence only of the secondary phase (ZnOMn$_3$) which is ferromagnetic but with Curie temperature around 50 K [43]. Based on that, we can conclude that the RT ferromagnetism in our samples could be related to the defects and to the substituting of Mn in the ZnO host rather than from the secondary phases of Mn. This explanation is corroborated by XRD result which shows an expansion of the unit cell volume with increasing Mn concentrations and the presence also of strain which affect the crystal quality. Therefore, more studies have to be done to understand the room-temperature ferromagnetism in TM-doped ZnO. Our synthesis method which was used also in recent work on Co-doped ZnO [44] encourages us to extend this work to other TM doped ZnO.

4 Conclusion

Nanocrystalline Zn$_{1-x}$Mn$_x$O powders have been synthesized by a simple sol–gel method. The synthesis protocol is based on a slow hydrolysis of the precursor using an esterification reaction, followed by a supercritical drying in EtOH. XRD results indicated that all the synthesized undoped and Mn-doped ZnO samples had the wurtzite structure. The lattice parameters 'a' and 'c' increase with the doping percentage of Mn increases which indicates that Mn^{2+} ions substitute Zn^{2+} ions. The crystallite size was calculated by Scherer formula and Williamson–Hall methods based on the XRD data. It was found that crystallite size decreases with increasing Mn concentration. Room temperature ferromagnetism is obtained for all samples and this ferromagnetic order might be related to the substituting of Mn in the ZnO host rather than from the secondary phases of Mn.

References

1. J.H. Li, D.Z. Shen, J.Y. Zhang, D.X. Zhao, B.S. Li, Y.M. Lu, Y.C. Liu, X.W. Fan, J. Lumin. **122**, 352 (2007)
2. U. Llyas, R.S. Rawat, G. Roshan, T.L. Tan, P. Lee, S.V. Springham, S. Zhang, L. Fengji, R. Chen, H.D. Sun, J. Appl. Surf. Sci. **258**, 890 (2011)
3. J. El Ghoul, C. Barthou, L. El Mir, J. Superlattices Microstruct. **51**, 942 (2012)

4. D.A.A. Santos, M.A. Macêdo, Physica B **407**, 3229 (2012)
5. T. Soki, Y. Hatanaka, D.C. Look, Appl. Phys. Lett. **76**, 3257 (2000)
6. S. Ezhilvalavan, T.R.N. Kutty, Mater. Chem. Phys. **47**, 258 (1997)
7. M. Karimi, J. Saydi, M. Mahmoodi, J. Seidi, M. Ezzati, S.S. Anari, B. Ghasemian, J. Phys. Chem. Solids **74**, 1392 (2013)
8. S. Fernández, A. Bollero, F.B. Naranjo, O. de Abril, J.J. Gandía, Vacuum **99**, 56 (2014)
9. C.R. Gorla, N.W. Emanetoglu, S. Liang, W.E. Mayo, Y. Lu, M. Wraback, H.J. Shen, J. Appl. Phys. **85**, 2595 (1999)
10. K.K. Nagaraja, S. Pramodini, A.S. Kumar, H.S. Nagaraja, P. Poornesh, D. Kekuda, Opt. Mater. **35**, 431 (2013)
11. S.J. Pearton, C.R. Abernathy, M.E. Overberg, G.T. Thaler, D.P. Norton, N. Theodoropoulou, A.F. Hebard, Y.D. Park, F. Ren, J. Kim, L.A. Boatner, J. Appl. Phys. **93**, 1 (2003)
12. S.S. Kim, J.H. Moon, B.T. Lee, O.S. Song, J.H. Je, J. Appl. Phys. **95**, 454 (2004)
13. T. Dietl, H. Ohno, F. Matsukura, J. Cibert, D. Ferrand, Science **287**, 1019 (2000)
14. T. Fukumura, Z. Jin, A. Ohtomo, H. Koinuma, M. Kawasaki, Appl. Phys. Lett. **75**, 3366 (1999)
15. A.S. Menon, N. Kalarikkal, S. Thomas, Indian J. NanoSci. **1**, 16 (2013)
16. H.K. Park, D.K. Kim, C.H. Kim, J. Am. Ceram. Soc. **80**, 743 (1997)
17. C. Jing, Y. Jiang, W. Bai, J. Chu, A. Liu, J. Magn. Magn. Mater. **322**, 2395 (2010)
18. L. El Mir, J. El Ghoul, S. Alaya, M.B. Salem, C. Barthou, H.J. von Bardeleben, J. Phys. B Condens. Matter **403**, 1770 (2008)
19. T.T. Kodas, Adv. Mater. **6**, 180 (1989)
20. S.W. Yoon, S.B. Cho, S.C. We, S. Yoon, B.J. Suh, H.K. Song, Y.J. Shin, J. Appl. Phys. **93**, 7879 (2003)
21. X. Yan, T. Itoh, S. Dai, Y. Ozaki, Y. Fang, J. Phys. Chem. Solids **74**, 1127 (2013)
22. C.O. Chey, O. Nur, M. Willander, J. Cryst. Growth **375**, 125 (2013)
23. P. Sharma, A. Gupta, K.V. Rao, F.J. Owens, R. Sharma, R. Ahuja, J.M. Obluillen, B. Johansson, G.A. Gehring, Nat. Mater. **2**, 673 (2003)
24. K. Omri, J. El Ghoul, O.M. Lemine, M. Bououdina, B. Zhang, L. El Mir, Superlattices Microstruct. **60**, 139 (2013)
25. K. Omri, J. El Ghoul, A. Alyamani, C. Barthou, L. El Mir, Physica E **53**, 48 (2013)
26. B.D. Cullity, *Elements of X-Ray Diffraction* (Addison-Wesley, Reading, MA, 1978), p. 102
27. L. El Mir, Z.B. Ayadi, H. Rahmouni, J. El Ghoul, K. Djessas, H.J. von Bardeleben, J. Thin Solid Films **517**, 6007 (2009)
28. L. El Mir, Z.B. Ayadi, M. Saadoun, K. Djessas, H.J. von Bardeleben, S. Alaya, J. Appl. Surf. Sci. **254**, 570 (2007)
29. S.W. Jung, S.J. An, G.C. Yi, C.U. Jung, S.I. Lee, S. Cho, Appl. Phys. Lett. **80**, 4561 (2002)
30. J. El Ghoul, C. Barthou, L. El Mir, Physica E **44**, 1910 (2012)
31. N. Tahir, S.T. Hussain, M. Usman, S.K. Hasanain, A. Mumtaz, Appl. Surf. Sci. **255**, 8506 (2009)
32. S. Yang, Y. Zhang, J. Magn. Magn. Mater. **334**, 52 (2013)
33. M. Bououdina, K. Omri, M. El-Hilo, A. El Amiri, O.M. Lemine, A. Alyamani, E.K. Hlil, H. Lassri, L. El Mir, Physica E **56**, 107 (2014)
34. O.D. Jayakumar, I.K. Gopalakrishnan, C. Sudakar, R.M. Kadam, S.K. Kulshreshtha, J. Alloys Compd. **438**, 258 (2007)
35. M.K. Sharma, R.N. Gayen, A.K. Pal, D. Kanjilal, R. Chatterjee, J. Alloys Compd. **509**, 7259 (2011)
36. M. El-Hilo, A.A. Dakhel, J. Magn. Magn. Mater. **323**, 2202 (2011)
37. A.M.A. Hakeem, J. Magn. Magn. Mater. **322**, 709 (2010)
38. D. Mukherjee, T. Dhakal, H. Srikanth, P. Mukherjee, S. Witanachchi, Phys. Rev. B **81**, 205202 (2010)
39. S. Chattopadhyay, S.K. Neogi, A. Sarkar, M.D. Mukadam, S.M. Yusuf, A. Banerjee, S. Bandyopadhyay, J. Magn. Magn. Mater. **323**(3–4), 363–368 (2011)
40. H.L. Yan, X.L. Zhong, J.B. Wang, G.J. Huang, S.L. Ding, G.C. Zhou, Y.C. Zhou, Appl. Phys. Lett. **90**, 082503 (2007)
41. J.J. Liu, K. Wang, M.H. Yu, W.L. Zhou, J. Appl. Phys. **102**, 024301 (2007)
42. R.K. Zheng, H. Liu, X.X. Zhang, V.A.L. Roy, A.B. Djurisie, Appl. Phys. Lett. **85**, 2589 (2004)
43. A.K. Pradhan, K. Zhang, S. Mohanty, J.B. Dadson, D. Hunter, J. Zhang, D.J. Sellmyer, U.N. Roy, Y. Cui, A. Burger, S. Mathews, B. Joseph, B.R. Sekhar, B.K. Roul, Appl. Phys. Lett. **86**, 152511 (2005)
44. J. El Ghoul, M. Kraini, O.M. Lemine, L. El Mir, J. Mater. Sci. Mater. Electron (2015). doi:10.1007/s10854-015-2732-x